PNAS
www.pnas.org

Supplementary Materials for

Mapping the temperature-dependent and network-site-specific onset of spectral diffusion at the surface of a water cluster cage

Nan Yang[1], Sean C. Edington[1], Tae Hoon Choi[2], Elva V. Henderson[2], Joseph P. Heindel[3], Sotiris S. Xantheas[3,4,*], Kenneth D. Jordan[2,*], and Mark A. Johnson[1,*]

[1]Sterling Chemistry Laboratory, Yale University, New Haven, CT 06520, USA

[2]Department of Chemistry, University of Pittsburgh, Pittsburgh, Pennsylvania 15260, USA

[3]Department of Chemistry, University of Washington, Seattle, WA, 98195, USA

[4]Advanced Computing, Mathematics and Data Division, Pacific Northwest National Laboratory, 902 Battelle Boulevard, P.O. Box 999, MS K1-83, WA, 99352, USA

*Authors to whom correspondence should be addressed:

Mark A. Johnson Email: mark.johnson@yale.edu

Kenneth D. Jordan Email: Jordan@pitt.edu

Sotiris S. Xantheas Email: Sotiris.Xantheas@pnnl.gov

This PDF file includes:

www.pnas.org/cgi/doi/10.1073/pnas.2017150117

Other supplementary material for this manuscript includes:

Frequency list MP2_aug-cc-pvDZ.xlsx

Spectral data.xlsx

XYZ coordinates MP2_aug-cc-pvDZ.xlsx

XYZ coordinates MP2_aug-cc-pvTZ.xlsx

water3_isomerization.mp4

water10_isomerization.mp4

Heat_capacity.txt (matlab script)

Internal_E_Distrubtion_sampling.txt (matlab script)

SI. Experimental Methods

A. Instrument overview and cluster formation. The instrument diagram is displayed in Fig. S5. $D_3O^+\cdot(HDO)(D_2O)_{19}$ cluster ions were obtained by first electrospraying 10 mM D_2SO_4 aqueous solution in a purge capsule humidified by the vapor pressure of a reservoir containing a 1:20 HDO:D_2O mixture. These clusters were passed through three stages of differential pumping and accumulated at high vacuum in Guide 2 (see Fig. S5) in preparation for pulsed injection into a temperature-controlled Paul trap kept at the experiment temperature (10-200 K in this study). Pulsed injection, as opposed to constant loading of the Paul trap, is crucial to establish a "synchronized" ensemble of cluster ions whose collective temperature-dependent behavior can be meaningfully measured as a function of time. Pulsed injection is also critical for in-trap mass selection: continued loading of ions after the mass selection pulse would defeat this initial mass selection stage.

B. Ion trap loading. The experiment cycle (100 ms duration) begins with a pulse of helium buffer gas, which is used to slow down the ions and thermally equilibrate them with the trap walls. The gas pressure quickly (< 5 ms) rises above the minimum pressure required for efficient ion trapping (~10^{-4} Torr) and then slowly pumps out. The gas pressure persists above the minimum trapping pressure for about 30 ms, after which ion trapping becomes very inefficient. Injection of the ion packet accumulated in Guide 2 into the Paul trap occurs ~5 ms after the beginning of the buffer gas pulse when trapping efficiency is maximum. The ion loading window and estimated trap pressure over time are illustrated in Fig. S7a. However, the residual gas pressure is still enough to sustain the thermal equilibrium throughout the 100 ms cycle. This is consistent with experiments performed on a protonated pentapeptide ion at 10 K using a similar instrument [32] which indicated residual buffer gas pressure maintained canonical behavior even ~70 ms after the gas pulse.

C. In-trap mass selection and ion packet storage. After the ion packet is injected and cooled, an amplitude-modulated frequency sweep (1-200 kHz, 2 V amplitude) is applied to one of the end caps of the Paul trap. When the waveform's frequency matches the secular frequency of an ion of a particular m/z, ions of that m/z will be ejected from the ion trap. In-trap mass selection can therefore be achieved through amplitude modulation (AM) of the frequency sweep. Specifically, waveform amplitude is reduced to zero as swept frequency approaches the secular frequency of the ion to be preserved (in this case $D_3O^+\cdot(HDO)(D_2O)_{19}$ ion with m/z=421), and is restored after the sweep passes this frequency. Waveform frequency over time, the AM pulse, and the output waveform are displayed in Fig. S7. After mass isolation of the $D_3O^+\cdot(HDO)(D_2O)_{19}$ species, ion packet is stored in the ion trap until the beginning of the Time-of-Flight (TOF) mass analysis, at which time the ion packet is extracted from the Paul trap into the TOF region.

D. Collection of infrared spectra without in-trap laser excitation. In a typical single laser experiment where the predissociation yield of all mass degenerate isotopomers is recorded, the m/z-selected ions are irradiated with a pulsed (10 Hz, 8 ns) tunable OPO/OPA IR laser (LaserVision) in the TOF region. This results in cluster dissociation via water loss upon resonant excitation of the m/z-selected ions. The fragment ions are isolated by a subsequent mass selection stage and recorded as a channel for detection of IR absorption.

E. Collection of isotopomer-selective, bleach-probe IR-IR spectra with in-trap laser excitation. Isotopomer-selective, two-color, IR-IR double resonance, hole burning dip spectra were acquired by first irradiating m/z-selected ions in the Paul trap with the bleach laser. This causes mass change through water molecule loss as clusters with resonant IR features absorb of one or more photons. The first TOF mass selection stage is used to eliminate the resulting fragments. The remaining parent ions are subsequently irradiated by the probe laser and separated again in the second and third TOF mass separation stages, where the photofragment from the probe laser is monitored. When acquiring an isotopomer-selective double resonance dip spectrum, the probe laser is fixed at a frequency where one or several similar isotopomers are known to absorb. The bleach laser is then scanned through the entire spectrum. When the

bleach laser dissociates the parent ion monitored by the probe laser, the probe fragment signal is reduced (bleached). This depletion is recorded as a function of bleach laser frequency. The resulting trace reveals the spectrum associated with the isotopomer selected by the probe. Irradiating the ions inside the ion trap enables variation of the delay between the bleach and the probe lasers and makes it possible to monitor reaction kinetics in systems of interest. The key is that both bleach and probe lasers remove ground state population by photodissociation (evaporation of a water molecule in this case, since bare clusters are excited in contrast to the typical "tagging" method that involves photodissociation of a weakly bound adduct like H_2 or Ar). [19]

F. Interpretation of bleach-probe IR-IR results in low- and high-temperature cases. At low temperatures where different isotopomers do not interconvert, the population depletion caused by the bleach laser remains the same over time (Fig. S8a, b). Thus, photodepletion of isotopomer B's population does not influence the population in A. However, photodepletion of A necessarily results in decrease in isotopomer A's (its own) population. When the probe laser is fixed on A and the bleach laser is scanned through the entire spectrum, there will only be a dip feature at the frequency corresponding to A regardless of the bleach-probe delay time. The time-dependent population is constant (Fig. S8c). Now consider the elevated temperature case where interconversion between isotopomers A and B can occur. Bleaching B will now result in a decrease in B's population which is, in turn, refilled by exchange with A's population. This ultimately results in depletion both A's and B's population (Fig. S8d). Similarly, photodepletion of A's population results in decrease of both the population of A and B over time (Fig. S8e). In that case, the hole-burning spectra at longer delay times display dip features at frequencies corresponding to both the A and B isotopomers (Fig. S8f) and the time dependence of the populations reveals their interconversion kinetics.

G. Isotopomer interconversion kinetics within the ion packet ensemble. The kinetics observed here reflect the ensemble behavior of many clusters held in the ion trap and thermally equilibrated with the trap wall through buffer gas collisions. The cluster ions behave as a thermodynamic canonical ensemble. For individual cluster ions, rare large amplitude motions rearrange the hydrogen bond network and result in interconversion between different isotopomers. If we consider the model system where type A and type B isotopomers interconvert with each other, we can follow the behavior of individual clusters (Fig. S9b). Initially (t=0), the system is in equilibrium and there are (for example) 3 clusters of type A and 6 of type B. This corresponds to an equilibrium constant of 2 for A↔B interconversion. As time passes, some type A isotopomers spontaneously become type B, and some type B isotopomers become type A, through H-bond switching. The overall population ratio remains the same since the system remains in equilibrium. Then, at t=15 ms, the bleach laser dissociates all clusters of type A and leaves behind the 6 type B clusters. As the equilibrium condition is compromised, it becomes more probable, overall, for type B clusters to convert into type A clusters. Thus, the population of B is gradually depleted and the population of A is partially restored (the cluster types statistically fluctuate, but on average some of the type B population is converted to type A). After a long waiting time, a new equilibrium is reached and the 6 remaining clusters are fractionated into 4 of type B and 2 of type A, preserving the equilibrium constant of 2. The ensemble average of population displays first order kinetics that can be expressed as an exponential decay of the difference between the old equilibrium population and the new equilibrium population (Fig. S9a).

H. Measurement of thermal evaporation kinetics. In addition to performing laser experiments, the apparatus as currently configured can measure thermal evaporation kinetics. After in-trap mass selection, the ions are stored at modest (see section B) vacuum inside the Paul trap. The delay time between the mass selection and the TOF mass analysis can be varied. The time-dependent populations of the parent ion and the evaporation products (smaller water clusters) reveal the water clusters' evaporation kinetics (Fig. S6a). Such experiments can be done at various temperatures to determine temperature-dependent evaporation rates. Yet another type of experiment can be done by applying a laser pulse immediately following mass selection. The absorption of a photon will result in a well-defined cluster internal energy

jump and consequent acceleration of evaporation. One can prepare clusters with the same average internal energy through either thermal heating or laser excitation. These methods should yield similar evaporation kinetics since IVR occurs on a timescale much faster than that of evaporation (Fig. S6b).

SII. Computational Methods for the Structures and Vibrational Frequencies of $H^+(D_2O)_{21}$

Detailed calculations on different H-bonding arrangements of $H_3O^+ \cdot (H_2O)_{20}$ with a pentagonal dodecahedral structure identify 10 structurally similar, low-energy isomers that are very close in energy (Fig. S1). These structures minimize the number of dangling hydrogens on adjacent water monomers while having no dangling hydrogens adjacent to the H_3O^+ monomer. Seven of these isomers are known from earlier studies.[36, 37] Optimizations of the structures of the ten low-energy isomers were performed using the DF-MP2 method,[38-43] where the "DF" indicates the use of density fitting, in conjunction with the aug-cc-pVDZ basis set.[44-49] The DF-MP2/aug-cc-pVDZ optimized structures were used to calculate harmonic vibrational frequencies and intensities at the same level of theory.[50] The geometries were then reoptimized at the DF-MP2/aug-cc-pVTZ[44-49] level, with the resulting structures being used for subsequent single-point calculations at the DF-MP2/aug-cc-pVQZ[44-49] level of theory. All calculations were done using the Molpro 2018 package.[51,52] Table S1 lists the relative energies of the ten isomers calculated at the DF-MP2/aug-cc-pVQZ level of theory.

Vibrational frequencies were calculated for all 43 possible locations of H on each isomer, including on the hydronium monomer, for a total of 430 sets of frequencies. For the individual structural isomers, the spread in the relative zero-point energies (ZPEs) for the different isotopomers is only about 70 cm^{-1}, or 0.2 kcal/mol. This is close to the differences in the relative ZPEs of the ten $H_3O^+ \cdot (H_2O)_{20}$ isomers considered here.

In generating the calculated spectra reported in the main body of the text and in Fig. S1, the frequencies were scaled by a factor of 0.96, which brings the calculated frequencies of the free OH transitions into close agreement with experiment. The OH stretch frequencies where the H atom is located on the hydronium monomer are ~400 cm^{-1} lower in energy than the lowest frequency HOD OH stretch vibrations, and thus are not included in the calculated spectra used for comparison with experiment. The spectra from the remaining 400 isotopomers are given equal weight. Given their closeness in energy this should be a reasonable assumption for clusters at temperatures near or above 100 K.

SIII. Fitting and Data Processing

Population decays in Fig.3 and Fig.S6 are fitted with a single exponential function of the form $P(t) = P_{eq} + \left(P(0) - P_{eq}\right)e^{-\frac{t}{\tau}}$, where P_{eq} is the equilibrium population at $t = \infty$, P(0) is the initial population at t = 0, and τ is the characteristic time constant.

The temperature dependent fractional depletion in Fig. 4 is fitted in Fig. S11, assuming first order kinetics and the Arrhenius rate equation. First the rate constant depends on the Arrhenius equation $k(T) = Ae^{-\frac{E_0}{k_B T}}$ where k is the temperature-dependent first order rate constant, A is the pre-exponential factor (experimentally determined by measuring the rate constant at a known temperature), E_0 is the activation energy and k_B is the Boltzmann constant. Then the population over time can be calculated with the equation $P(t) = P_{eq} + \left(P(0) - P_{eq}\right)e^{-k(T)t}$ and the fractional depletion is $f = \frac{P(t)}{P_{pre}}$, where P_{pre} denotes the population before the bleach laser interaction.

SIV. Computational Results for $(H_2O)_{21}$

Figure S12 shows the 3D structure and the 2D Schlegel diagram[54] of the lowest energy isomer of $(H_2O)_{21}$ with a PD cage and internal H_2O molecule identified to date.[53] The Schlegel diagram indicates the numbering of the water molecules used in this work.

Figure S13 displays the lowest energy pathways for rotation of each of the AAD molecules of $(H_2O)_{21}$. These results were obtained using the MB-pol potential[55] and were provided by D. Wales. They were confirmed by our own calculations carried out using the OPTIM code.[56] Note that each of these pathways involves two or three transition state structures, and, hence, one or two intermediate structures. All pathways include at least one 4-membered ring in the intermediate, except in the case of water 15 where the 4-membered ring appears in a TS. Additionally, at least one intermediate in each pathway, except in the case of water 4, includes a 5-coordinated water in the local minimum.

Figure S14 depicts using Schlegel diagrams the lowest energy rotational pathway (involving water 3) of $(H_2O)_{21}$. Movies depicting this rearrangement process and that for water 10 are in the supplemental files 'water3_isomerization.mp4' and 'water10_isomerization.mp4'.

Table S2 reports the energies of the stationary points on the pathways for rotating each of the eight AAD water molecules of $(H_2O)_{21}$. Results are reported for the TTM-2.1-F [57] and MB-pol force fields, and in a subset of cases, also at the MP2/aug-cc-pVDZ level of theory. Vibrational zero-point energy (ZPE) corrections of the $(HOD)(D_2O)_{20}$ isoptopomers, calculated in the harmonic approximation are also indicated.

Table S3 reports the harmonic OH stretch frequencies of the $HOD(D_2O)_{20}$ cluster for each of the 21 locations of the HOD molecule and for both possible isotopomers in each case. These results were obtained using the MB-pol force field. Frequencies scaled by a factor of 0.95, to account approximately for the impact of vibrational anharmonicity, are also reported.

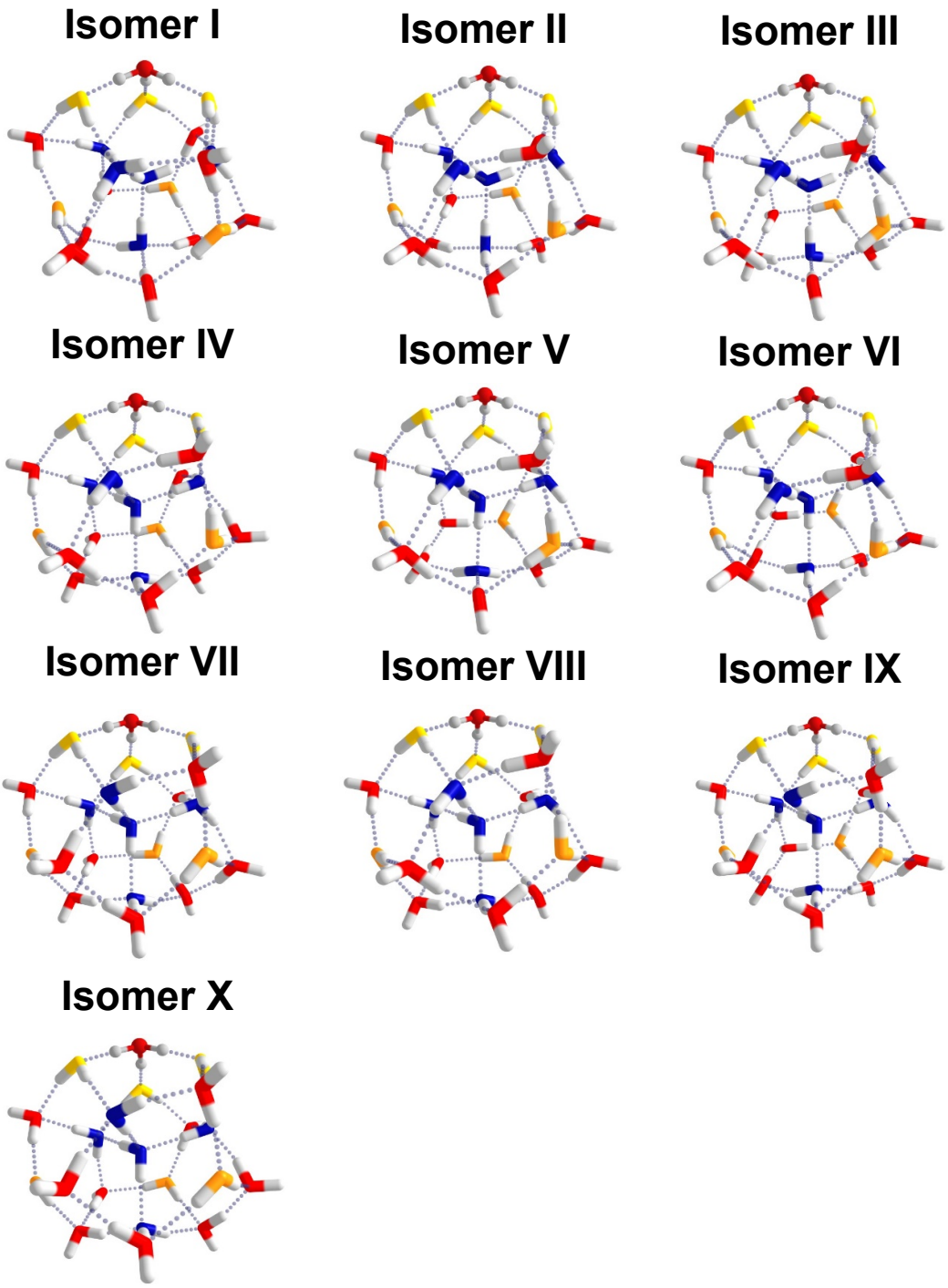

Fig. S1. Structures of 10 low energy isomers of the $H_3O^+ \cdot (H_2O)_{20}$ species. These geometries are optimized at the DF-MP2/aug-cc-pVTZ level.

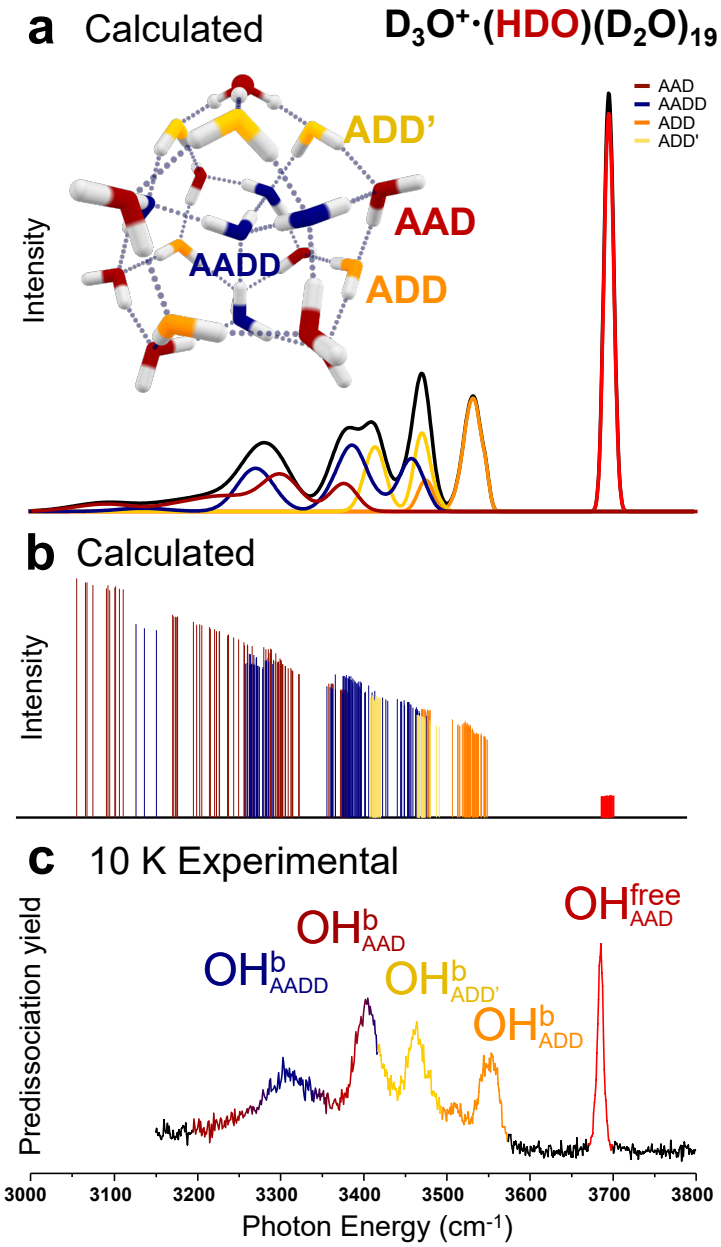

Fig. S2. Comparison between calculated and experimental vibrational spectra of isotopomers of the $D_3O^+\cdot(HDO)(D_2O)_{19}$ isotopologue. (a) Calculated spectra including summed contributions (black trace) from 400 isotopomers of the 10 low energy structural isomers shown in Fig. S1 where scaled (0.96 scaling factor) harmonic frequencies are convolved with experimentally determined linewidths (28). Contributions from the various types of water molecules are displayed in color coded traces that correspond to the scheme depicted in the representative structure. (b) Calculated stick spectra. (c) Experimental spectrum at 10 K including contributions of all isotopomers present.

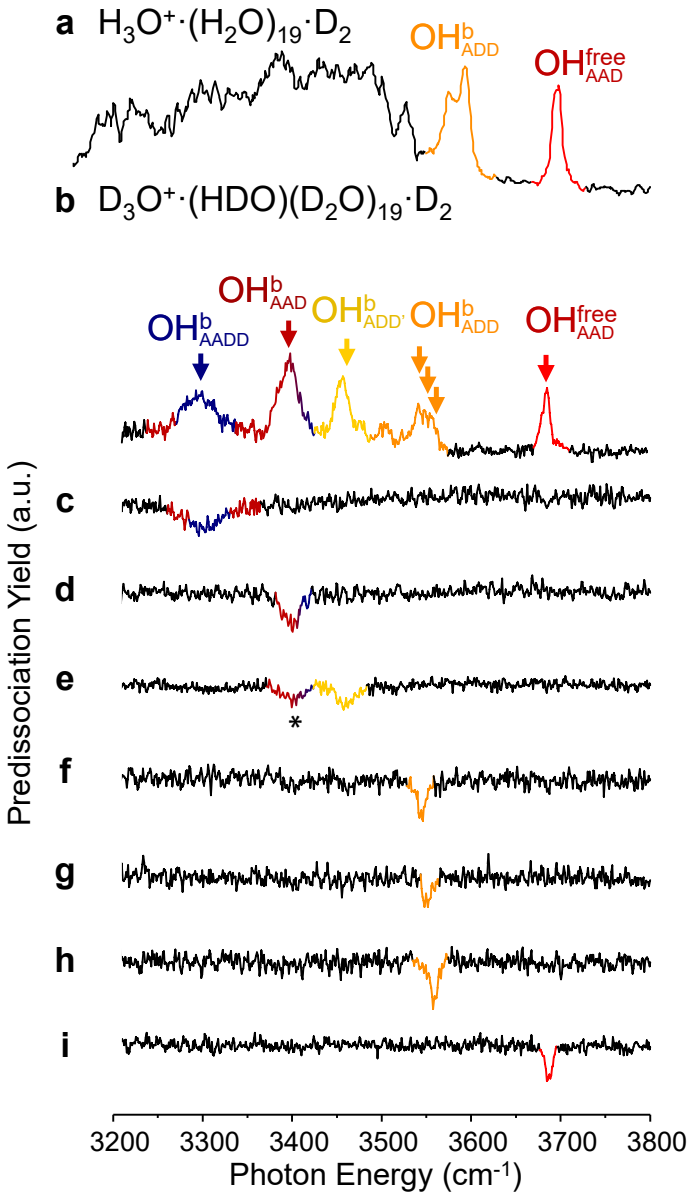

Fig. S3. Comparison between the vibrational spectra of $H_3O^+\cdot(H_2O)_{20}$ and $D_3O^+\cdot(HDO)(D_2O)_{19}$. Single laser vibrational predissociation spectra of the all-H isotopologue (a) and the $D_3O^+\cdot(HDO)(D_2O)_{19}$ isotopologue (b) obtained with the D_2 messenger tagging technique at 13.5 K. The single laser spectrum in (b) contains contributions from various isotopomers that are isolated with the isotopomer-specific double resonance hole burning technique and displayed in (c-i) where the probe position is indicated in (b) and color coded in the same scheme as Fig.1. The appearance of the lower energy feature in (e), denoted by *, was discussed previously in ref. 16 and attributed to combination band activity.

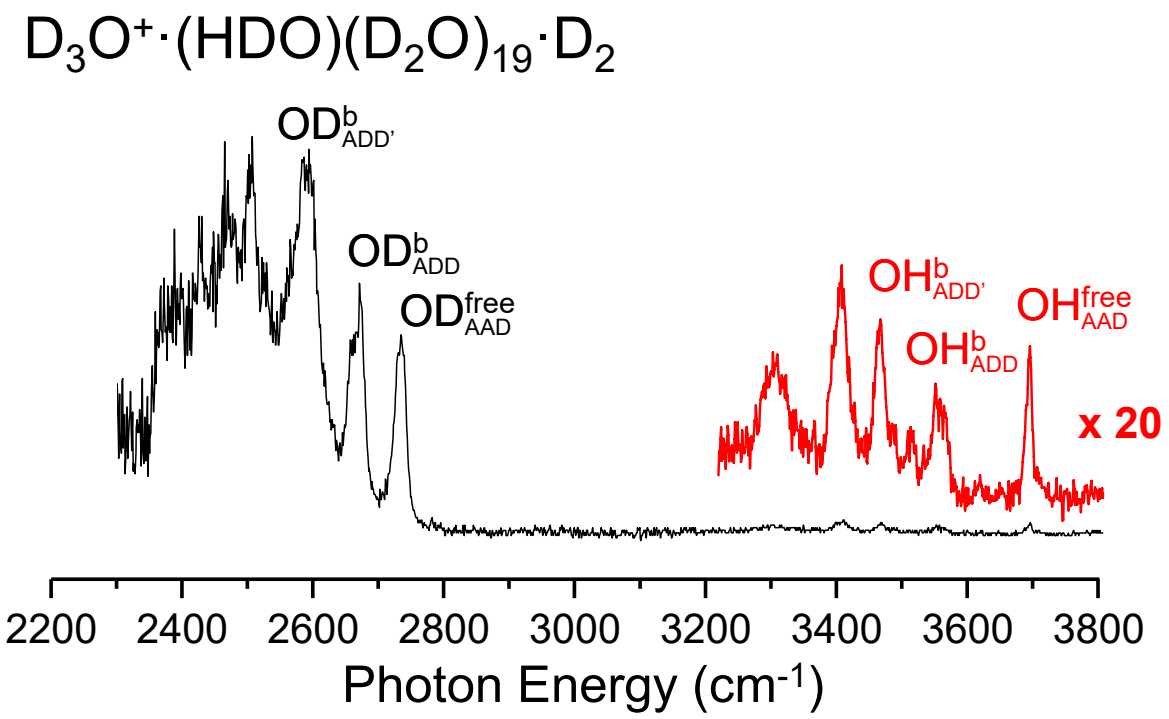

Fig. S4. Comparison of OD and OH stretching regions of the $D_3O^+\cdot(HDO)(D_2O)_{19}$ cluster. The red trace is a scaled up (by 20 times) version of the black trace in the OH region. The low intensity in the OH region is caused by isotopic dilution. As a result, each individual cluster displays 42 OD features and only one OH feature.

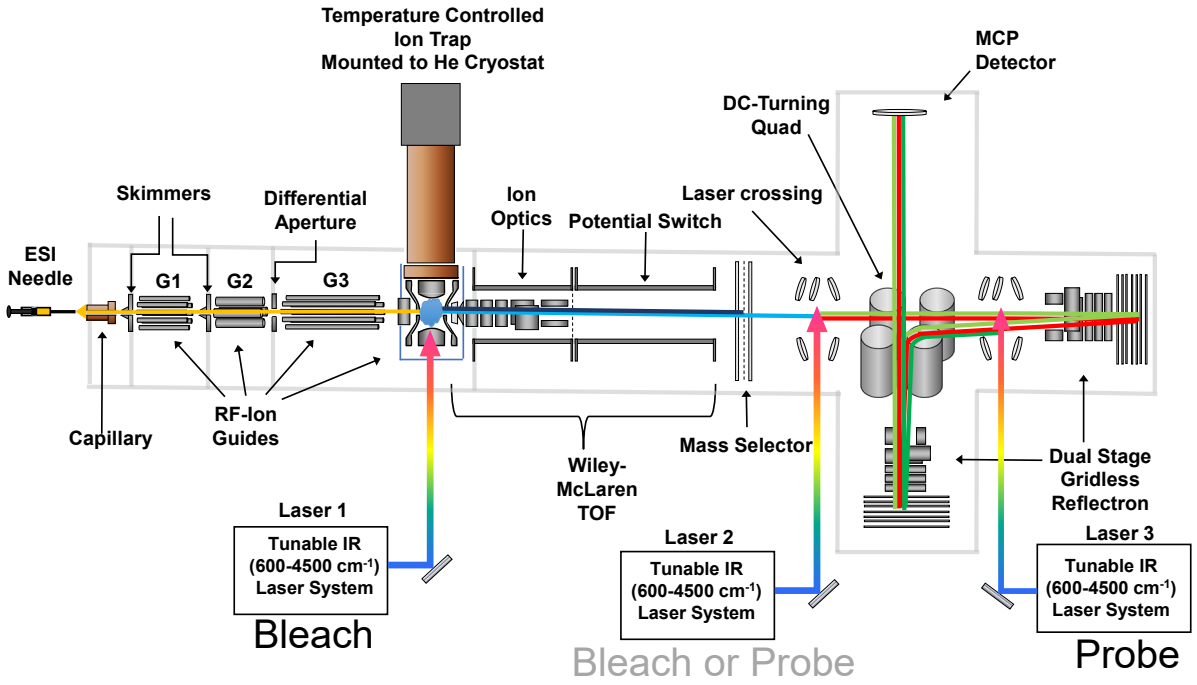

Fig. S5. MS^4IR^3 Instrument for the temperature controlled, variable delay time hole burning experiment. The instrument combines a custom ESI source, cryogenic ion trap (Paul trap), three laser interaction regions, and four stages of mass selection. The second ion guide (G2) is capable of storing ions and ejecting them as an ion packet into the Paul trap where secular frequency mass selection (MS^1) is performed. The bleach laser (IR^1) is introduced into the ion trap after ion cooling and mass selection. The bleached ion ensemble is stored for a variable delay time, then mass selected again (MS^2), this time with a Time-of-Flight mass analyzer. In the Time-of-Flight region there are two additional stages of mass selection with two reflectrons (MS^3 and MS^4). In between $MS^{2,3 \text{ and } 4}$ there are two IR lasers that can serve as the probe laser (Laser 2 and Laser 3). In this study, we use the in-trap laser and the third laser as the bleach and probe laser, respectively.

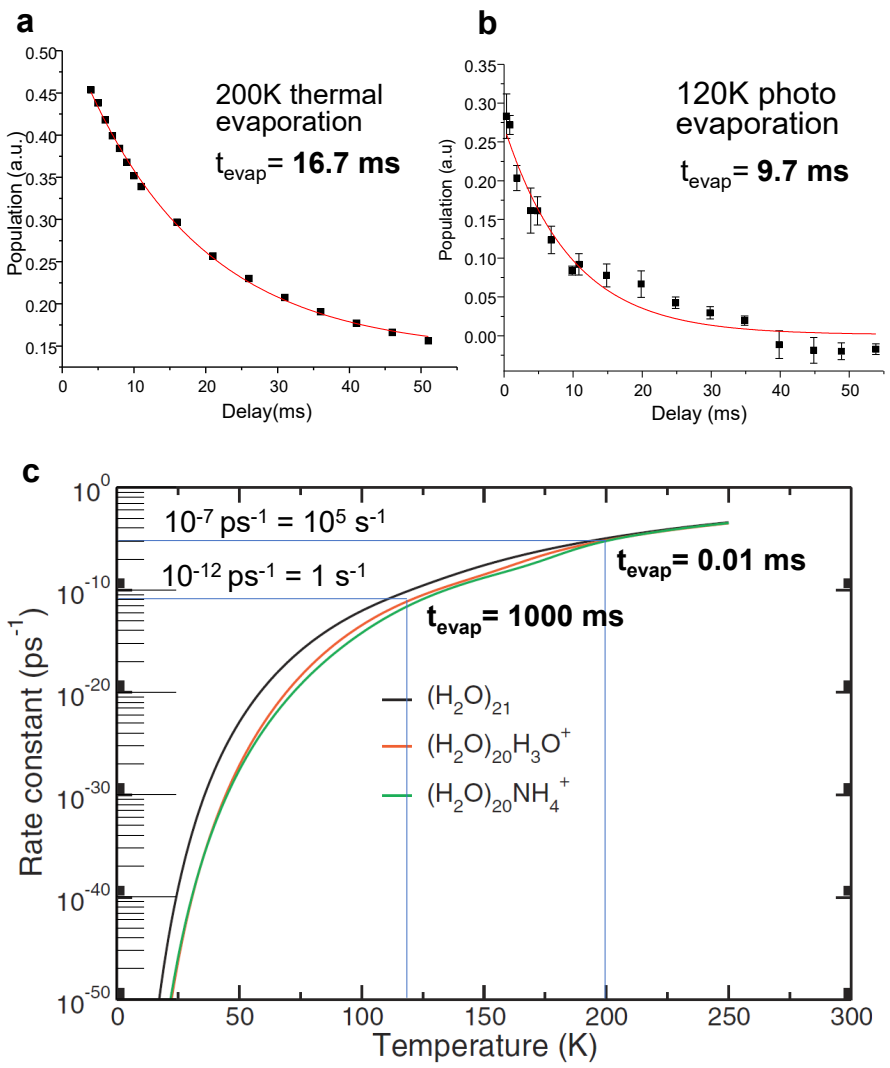

Fig. S6. Thermal and photo induced evaporation kinetics of the D_3O^+·(HDO)$(D_2O)_{19}$ clusters. (a) Thermal evaporation kinetics at 200 K measured in the Paul trap held at 200 K. The evaporation time is about 16.7 ms. The exponential behavior indicates that a canonical thermodynamic condition is established in the ion trap. (b) Photoinduced evaporation kinetics with vibrational excitation at 3,686 cm^{-1}, measured in the Paul trap held at 120 K. The evaporation time is about 450 ms without laser excitation and 9.7 ms with the laser excitation. The vibrational excitation heats the cluster to about 200 K, estimated using the harmonic heat capacity (Fig. S10). The experimentally measured rates agree qualitatively with the theoretically calculated rate constants (c) at 200 K. [26] Panel (c) is reprinted from ref. 26, with the permission of AIP Publishing.

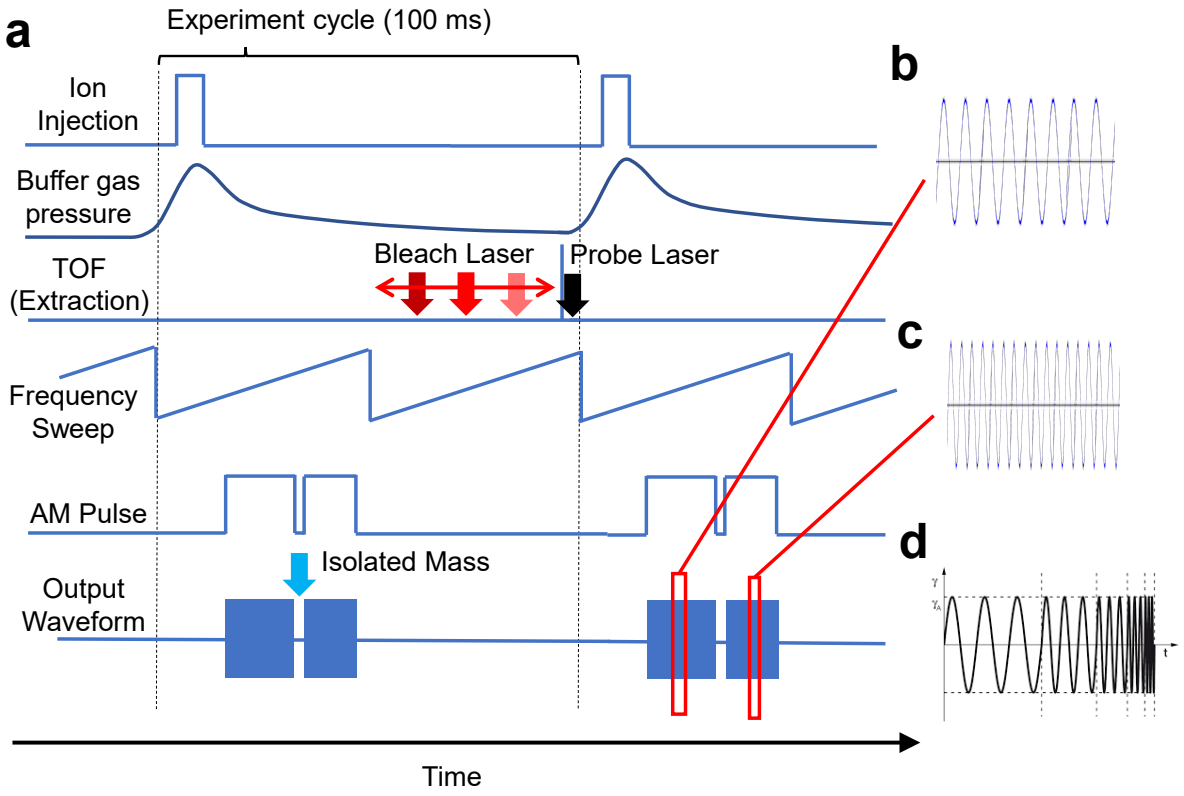

Fig. S7. Time sequence for the in-trap mass selection and variable delay two laser experiment. (a) The experiment starts with pulsed buffer gas and ion injection. After the ions are introduced and cooled in the Paul trap, an amplitude-modulated frequency sweep in the ion secular frequency range is introduced to select the desired mass. The frequency sweep (d) starts from low frequency that corresponds to the higher masses (b) and sweeps to high frequency (c) that removes the lower masses. The output waveform is modulated to zero when the frequency matches the desired mass to allow the target species to remain in the trap. After mass selection, the bleach laser is introduced to the trap at variable delay time. Finally, the ions are extracted from the ion trap for Time-of-Flight mass analysis and probe laser detection.

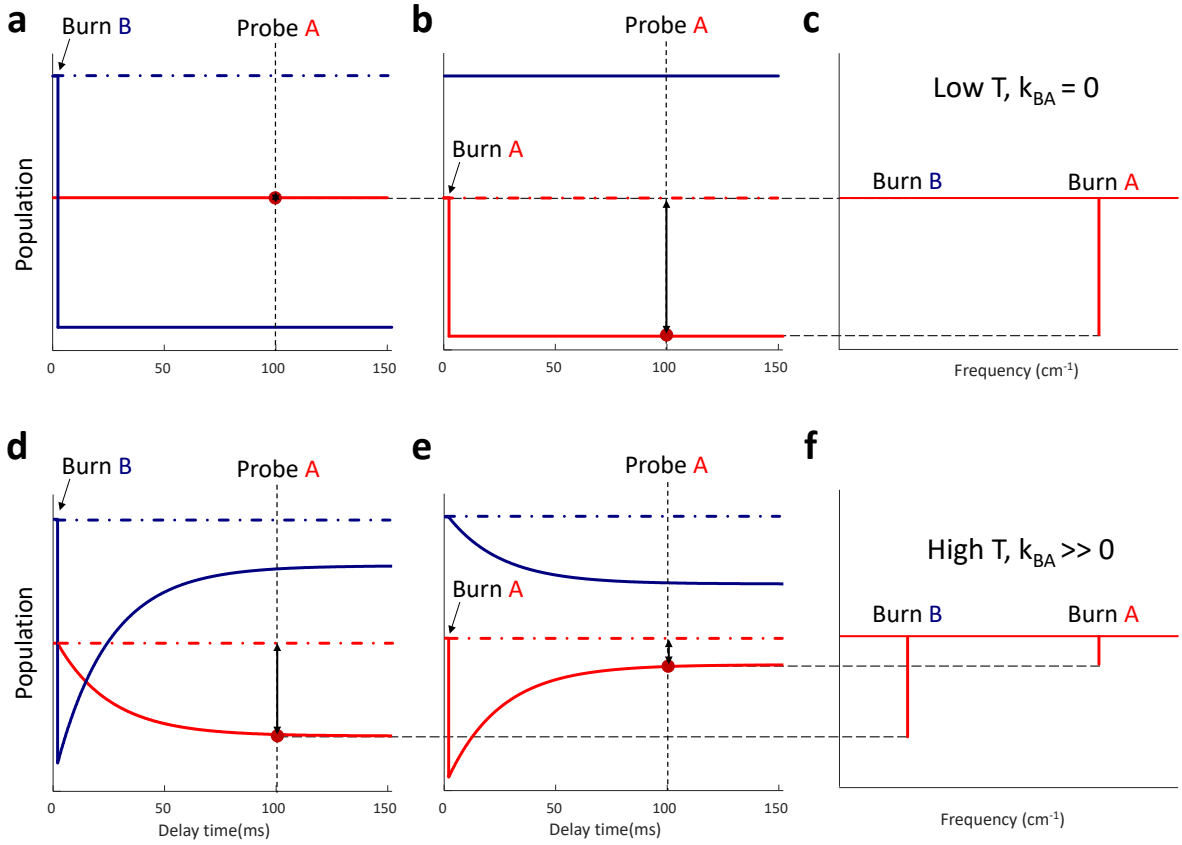

Fig. S8. Time dependent population behavior of a two isotopomer system at two different temperatures. (a-c) At low temperature, bleaching isotopomer B does not influence the population in A whereas bleaching A results in depletion of A's population at the frequency corresponding to A. (d-f) At higher temperatures where interconversion between the two isotopomers can happen, bleaching B will result in a decrease in A's population over time to refill the hole burned in B. Bleaching A will result in a large initial depletion in A, which is then refilled by B. This behavior manifests in the hole-burning spectra of A as two dips at both A's and B's positions.

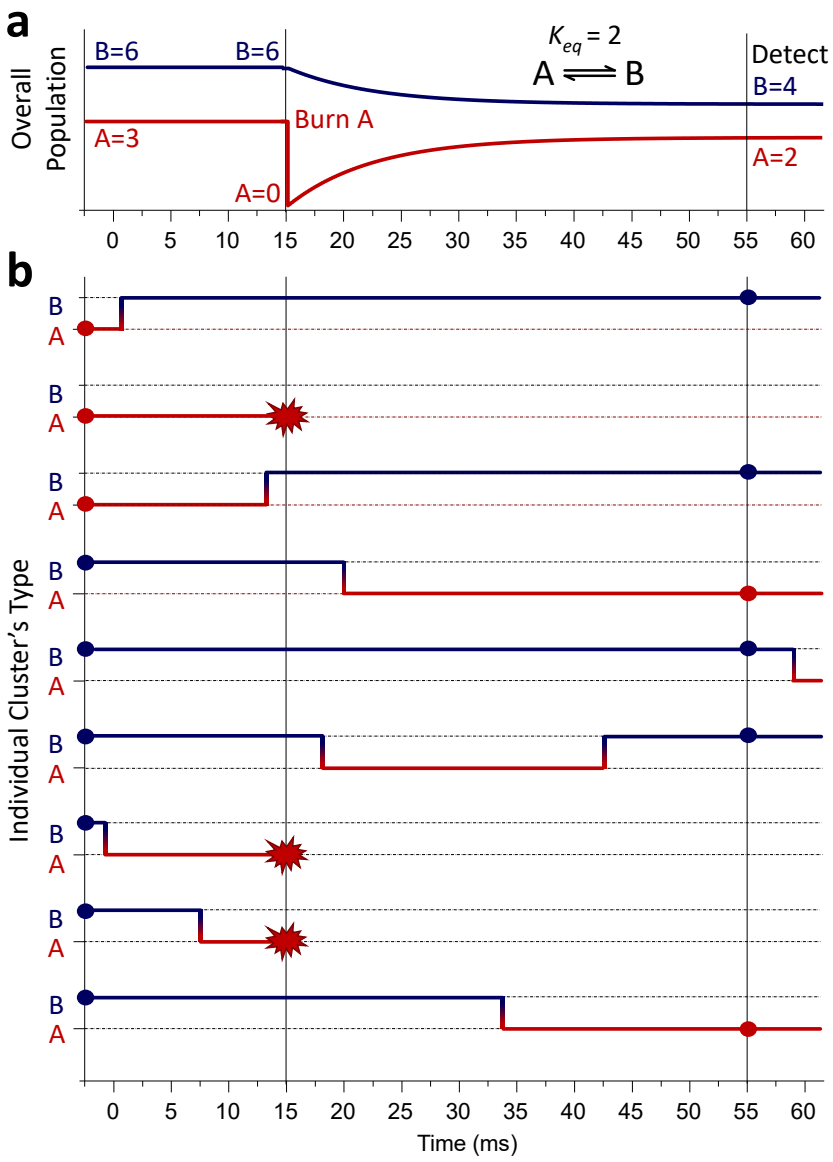

Fig. S9. Comparison between the ensemble behavior and the individual cluster ion's behavior at elevated temperature where interconversion between two isotopomers is possible. (a) The overall behavior of the ensemble including population in A and B isotopomers with an equilibrium constant of 2, which results in an equilibrium population ratio of 1:2 for A:B. (b) Behavior of nine individual clusters where interconversion between A and B is occurring spontaneously. The identity of the cluster is traced over time. Interconversion is depicted as a sudden jump from dotted line labeled A to B or vice versa. At t=15 ms, a bleach laser pulse is introduced at a frequency corresponding to absorption in isotopomer A, which destroys all instantaneous population in isotopomer A. At t=55 ms, the probe laser can be introduced to determine the population in A or B isotopomers.

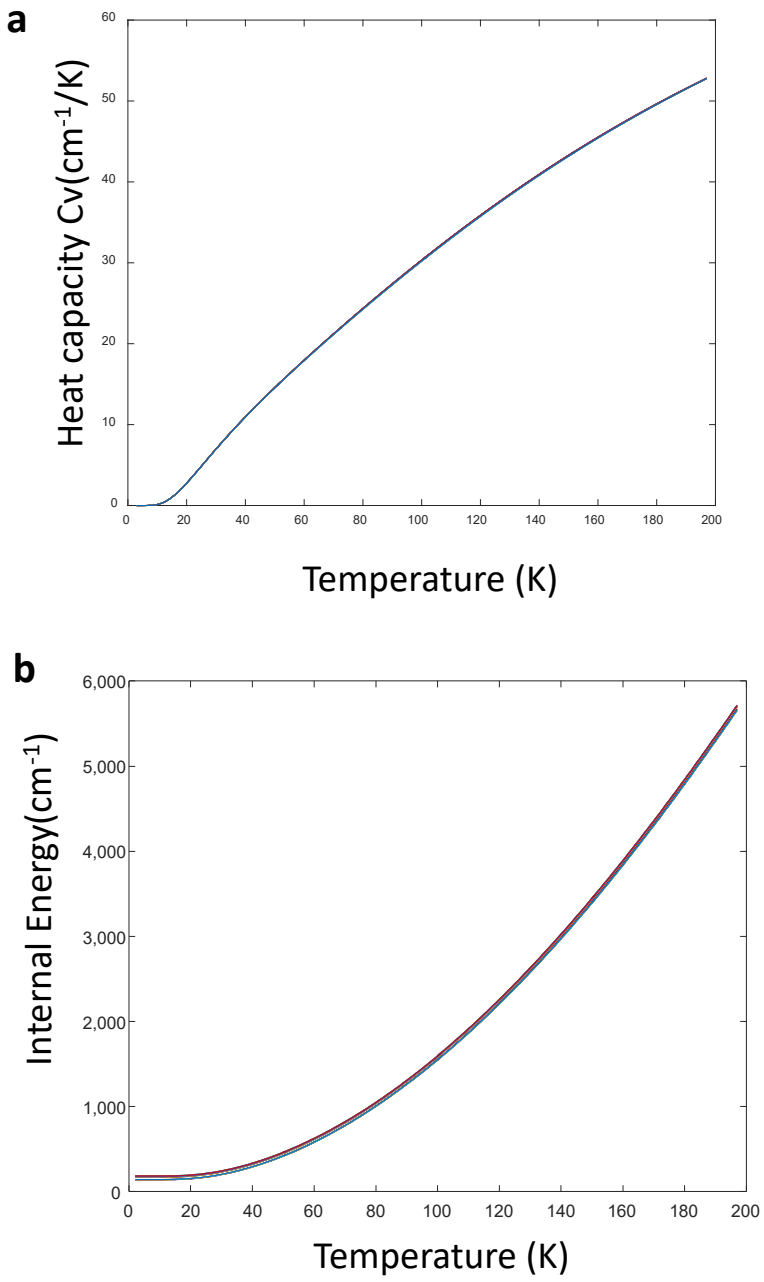

Fig. S10. Harmonic heat capacity curve and internal energy as a function of temperature for D_3O^+·(HDO)$(D_2O)_{19}$. The heat capacity (a) and internal energy (b) are similar among isotopomers. The scripts for calculating the internal energy, energy distribution, and heat capacity are collected in the supplementary files 'Heat_capacity.m' and 'internal_E_Distribution_sampling.m'.

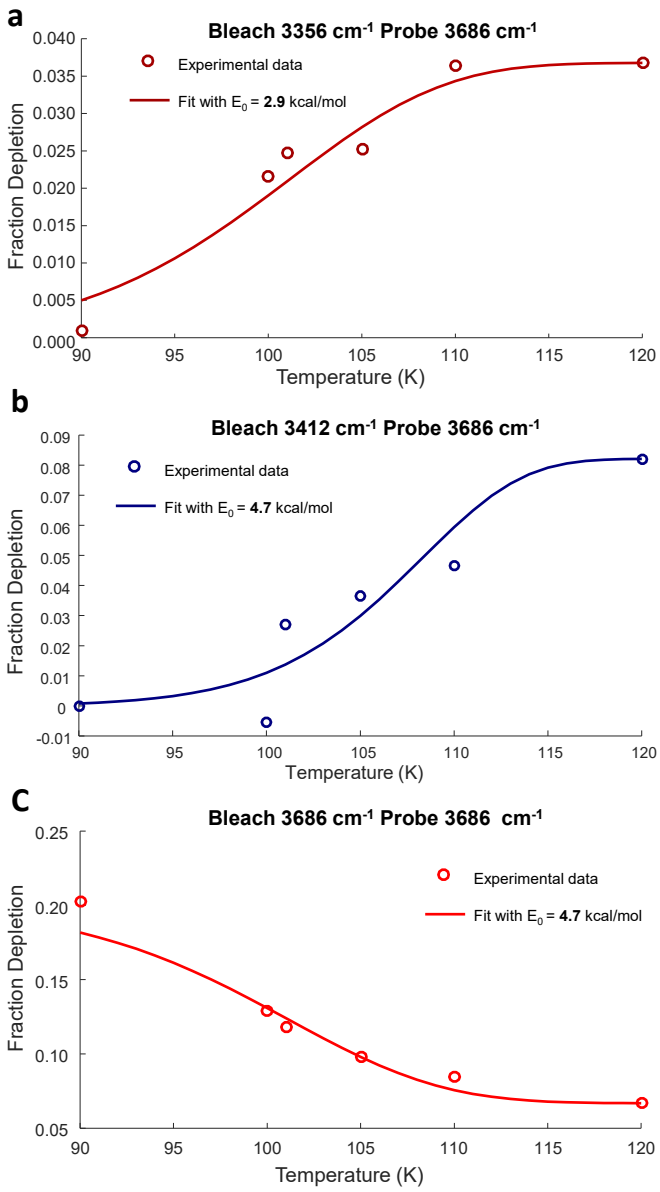

Fig. S11. Fractional depletion obtained at specific bleach-probe frequencies as a function of temperature. (a)Temperature dependent fractional depletion obtained at 50 ms delay time by probing the free OH position (3686 cm^{-1}) and bleaching the bound OH position of one of the AAD water molecules. This position has the lowest onset temperature for H-bond rearrangement and yields an apparent activation energy (E_0) of 2.9 kcal/mol (1000 cm^{-1}). (b, c) Temperature dependent fractional depletion obtained at 50 ms delay time by probing the free OH position (3686 cm^{-1}) and bleaching the bound OH position of one of the AADD water molecules (b) and bleaching the free OH position of all AAD water molecules (c). Both results yield an apparent activation energy (E_0) of ~4.7 kcal/mol (1670 cm^{-1}) which is consistent with the higher onset temperature (120 K) for all the other rearrangement pathways. The fit equation is discussed in the section SIII.

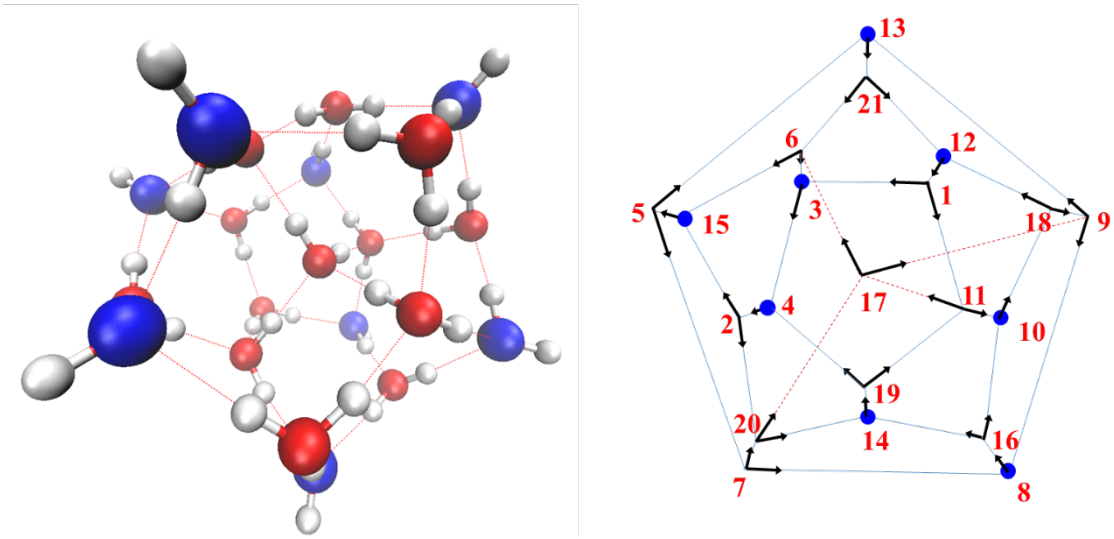

Figure S12. 3D structure and the 2D Schlegel diagram of the lowest energy isomer of $(H_2O)_{21}$. On the Schlegel diagram (right panel, a 2D projection of the 3D structure), each red number labels a water molecule's oxygen atom and black arrows point along the OH bond. Dotted red lines and thin blue lines are hydrogen bonds. Blue balls in the 3D structure (left panel) and blue dots in the Schlegel diagram (right panel) denote water molecules with a free OH group.

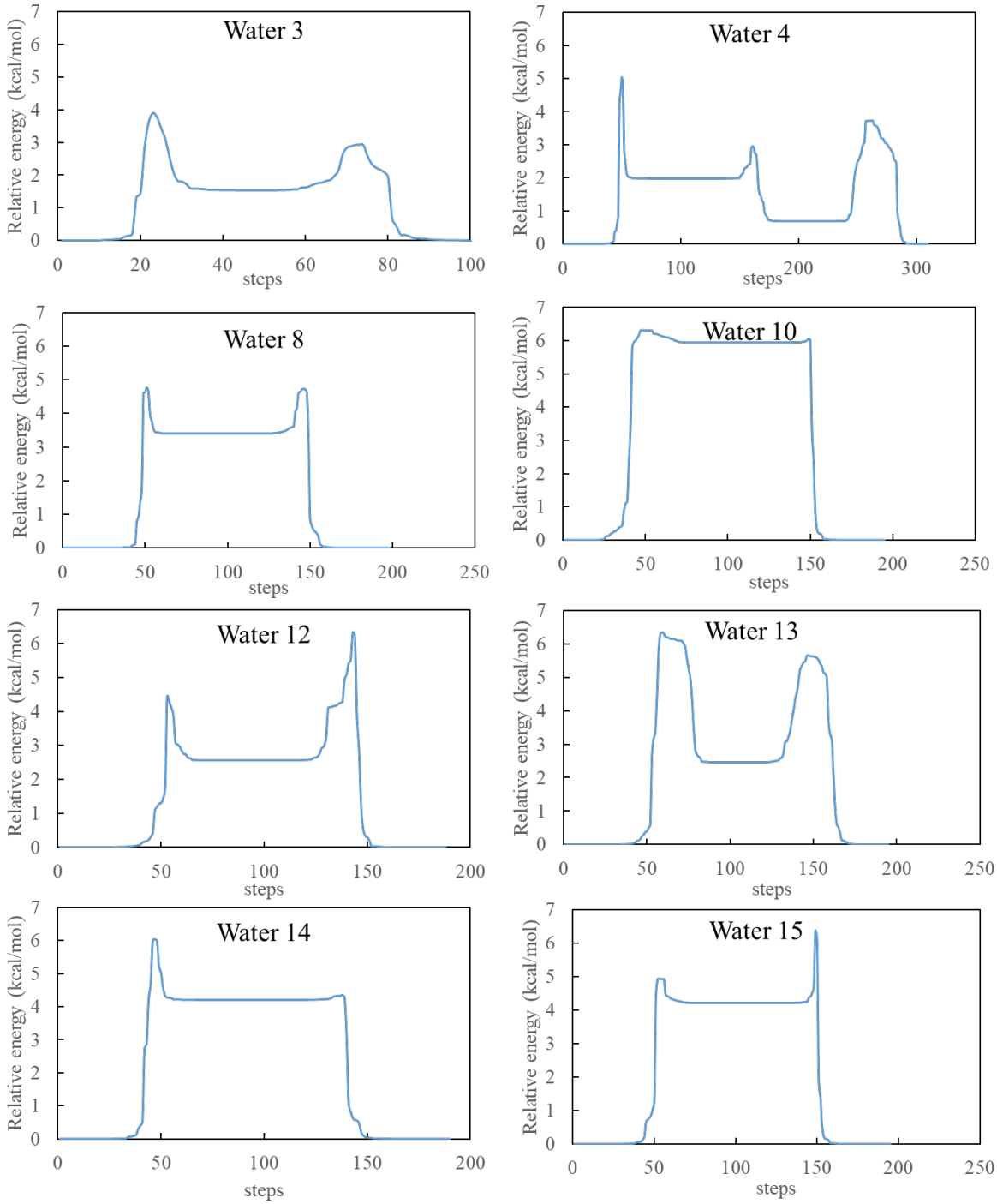

Figure S13. The lowest energy pathways for rotation of each of the AAD molecules of $(H_2O)_{21}$. The relative energies are calculated with MBPol. Movies depicting this rearrangement process for water 3 and that for water 10 are in the supplemental files 'water3_isomerization.mp4' and 'water10_isomerization.mp4'.

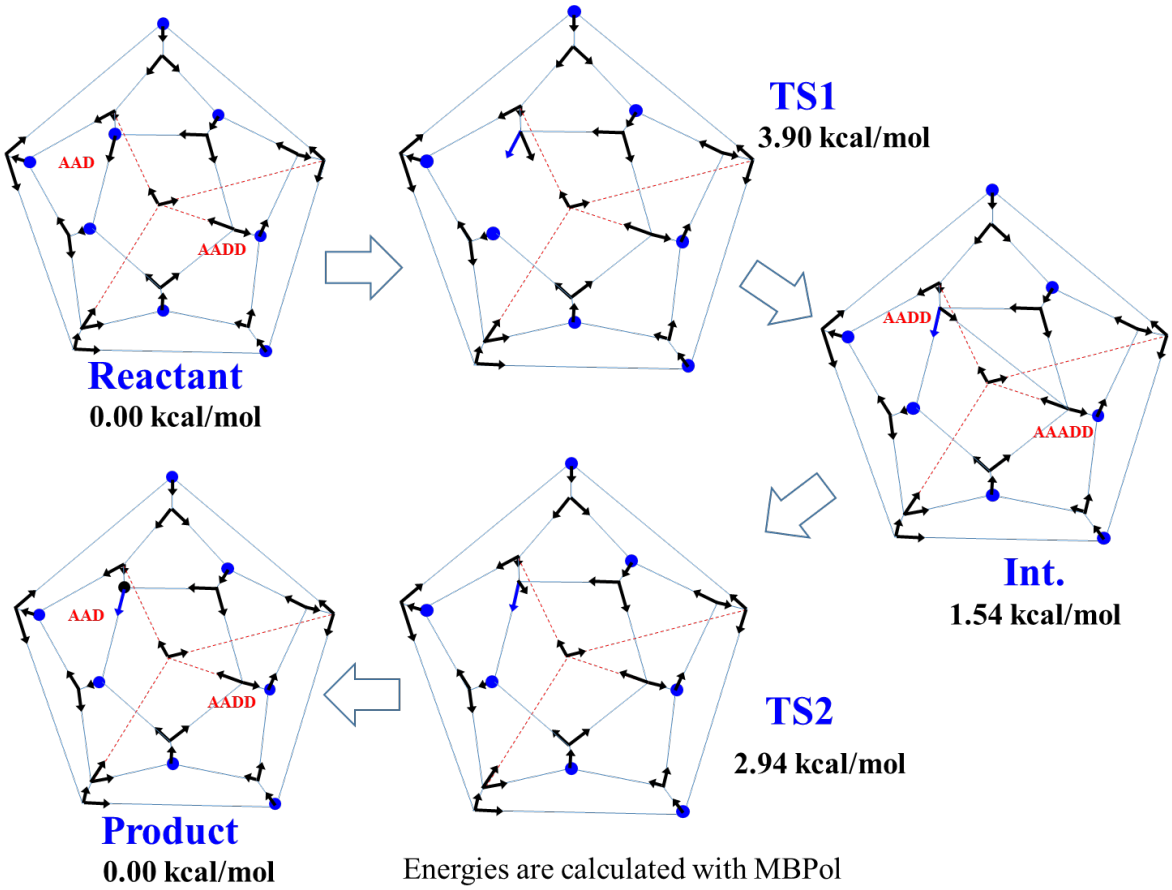

Figure S14. Schlegel diagrams for the lowest energy rotational pathway of water 3 (see Figure S12) of $(H_2O)_{21}$. The blue dots denote water molecules with a free OH group, the arrows label OH groups and the thinner lines represent hydrogen bonds. The water molecule labeled AAD in the reactant panel is the water molecule of interest that rearranges to exchange its free and bound OH groups. One of the original AAD water molecule's OH (black arrow) forms an additional hydrogen bond to the original AADD water molecule to form a four-membered ring involving a five coordinated AAADD water molecule.

Table S1. Relative energies of the lowest energy isomers of $H_3O^+ \cdot (D_2O)_{20}$. Energies are calculated at the DF-MP2/aug-cc-pVQZ level of theory, using geometries optimized at the DF-MP2/aug-cc-pVTZ level.

Isomer	Relative energy (kcal/mol)
1	0.082
2	0.049
3	0.029
4	**0.000**
5	0.021
6	0.075
7	0.137
8	0.034
9	0.134
10	0.161

Table S2. Energies (kcal/mol) of transition states and intermediates for rotating the water molecules of $(H_2O)_{21}$ with a free OH group. Energies are referenced relative to the global minimum.

Pathway	Method	TS 1	Int. 1	TS 2	Int. 2	TS 3
Water 3	TTM	4.73	1.50	2.70	-	-
	TTM + ZPE	3.61	0.78	2.08	-	-
	MBPol	3.90	1.54	2.94	-	-
	MBPol + ZPE	3.56	1.56	2.71	-	-
	MP2/AVDZ	-	2.20	-	-	-
Water 4	TTM	4.39	0.65	2.46	1.84	5.50
	TTM + ZPE	3.30	0.51	2.07	1.44	5.33
	MBPol	3.73	0.69	2.96	1.98	5.04
	MBPol + ZPE	3.35	0.70	2.78	2.11	4.69
	MP2/AVDZ	-	0.80	-	2.19	-
Water 8	TTM	6.06	2.92	4.00	-	-
	TTM + ZPE	4.78	2.85	3.37	-	-
	MBPol	4.77	3.41	4.73	-	-
	MBPol + ZPE	4.47	3.41	4.38	-	-

	MP2/AVDZ	-	3.57	-	-	-
Water 10	TTM	6.63	5.19	6.84	-	-
	TTM + ZPE	5.39	4.75	6.07	-	-
	MBPol	6.06	5.95	6.32	-	-
	MBPol + ZPE	5.75	5.74	5.90	-	-
	MP2/AVDZ	-	5.47	-	-	-
Water 12	TTM	5.31	2.45	5.00	4.75	5.46
	TTM + ZPE	4.32	2.03	4.99	4.81	5.35
	MBPol	6.34	2.56	4.14	4.03	4.46
	MBPol + ZPE	5.91	2.71	3.95	3.89	4.09
	MP2/AVDZ	-	3.29	-	4.77	-
Water 13	TTM	7.00	2.20	7.00	-	-
	TTM + ZPE	5.76	1.52	6.36	-	-
	MBPol	5.66	2.46	6.34	-	-
	MBPol + ZPE	5.12	2.44	5.98	-	-
	MP2/AVDZ	-	2.48	-	-	-
Water 14	TTM	4.90	3.88	4.91	-	-
	TTM + ZPE	3.69	3.20	4.57	-	-
	MBPol	6.04	4.21	4.36	-	-
	MBPol + ZPE	5.73	4.04	4.00	-	-
	MP2/AVDZ	-	4.93	-	-	-
Water 15	TTM	7.06	3.84	4.38	-	-
	TTM + ZPE	5.68	3.39	4.37	-	-
	MBPol	6.38	4.22	4.94	-	-
	MBPol + ZPE	5.95	4.15	4.61	-	-
`	MP2/AVDZ	-	4.64	-	-	

Table S3. Vibrational frequencies (cm^{-1}) of $(HOD)(H_2O)_{20}$ calculated in the harmonic approximation using the MB-pol model. Scaled frequencies, obtained by reporting the harmonic frequencies by 0.95 are also reported.

Water	Unscaled	Scaled
1	3609.95	3429.45
	3762.75	3574.61
2	3719.67	3533.68
	3589.7	3410.21
3	3897.43	3702.56
	3535.8	3359.01
4	3256.91	3094.07
	3889.42	3694.95
5	3539.59	3362.61
	3727.86	3541.47
6	3701.74	3516.65
	3628.93	3447.49
7	3679.73	3495.74
	3770.73	3582.19
8	3392.05	3222.45
	3901.49	3706.42
9	3668.29	3484.88
	3639.39	3457.42
10	3320.2	3154.19
	3907.18	3711.82
11	3680.73	3496.69
	3499.5	3324.53

Water	Unscaled	Scaled
12	3891.04	3696.49
	3383.25	3214.09
13	3328.79	3162.35
	3905.11	3709.86
14	3903.47	3708.29
	3361.55	3193.47
15	3905.56	3710.28
	3260.13	3097.13
16	3700.47	3515.44
	3694.43	3509.71
17	3556.16	3378.35
	3539.85	3362.86
18	3682.72	3498.58
	3661.88	3478.78
19	3721.98	3535.88
	3615.29	3434.52
20	3686.24	3501.93
	3520.99	3344.94
21	3665.99	3482.69
	3692.44	3507.82

SV. Coordinates of the Optimized Structures of the Ten Low-lying Isomers of $H_3O^+\cdot(H_2O)_{20}$

The coordinates and energy for the 10 low-lying isomers of $H_3O^+\cdot(H_2O)_{20}$ are collected in the supplementary files 'XYZ coordinates MP2_aug-cc-pvTZ.xlsx', and 'XYZ coordinates MP2_aug-cc-pvDZ.xlsx'.

SVI. Harmonic frequencies for $D_3O^+ \cdot (HDO)(D_2O)_{19}$

The harmonic frequencies for the 10 low-lying isomers (each includes 43 isotopomers) of $D_3O^+ \cdot (HDO)(D_2O)_{19}$ are collected in the supplementary file 'Frequency list MP2_aug-cc-pvDZ.xlsx'.

SVII. Supplementary Videos:

water3_isomerization.mp4: Movie depicting the rearrangement process for AAD water 3 shown in Fig.S13.

water10_isomerization.mp4: Movie depicting the rearrangement process for AAD water 10 shown in Fig.S13.

References

1. Brancato G, Rega N, Barone V. A hybrid explicit/implicit solvation method for first-principle molecular dynamics simulations. *Journal of Chemical Physics* 2008, **128**(14).

2. Fattebert JL, Lau EY, Bennion BJ, Huang P, Lightstone FC. Large-Scale First-Principles Molecular Dynamics Simulations with Electrostatic Embedding: Application to Acetylcholinesterase Catalysis. *Journal of Chemical Theory and Computation* 2015, **11**(12)**:** 5688-5695.

3. Price WD, Schnier PD, Jockusch RA, Strittmatter EF, Williams ER. Unimolecular reaction kinetics in the high-pressure limit without collisions. *J Am Chem Soc* 1996, **118**(43)**:** 10640-10644.

4. Xantheas SS. Low-lying energy isomers and global minima of aqueous nanoclusters: Structures and spectroscopic features of the pentagonal dodecahedron $(H_2O)_{20}$ and $H_3O^+(H_2O)_{20}$. *Can J Chem Eng* 2012, **90**(4)**:** 843-851.

5. Tian CS, Shen YR. Isotopic Dilution Study of the Water/Vapor Interface by Phase-Sensitive Sum-Frequency Vibrational Spectroscopy. *J Am Chem Soc* 2009, **131**(8)**:** 2790-2791.

6. Laage D, Stirnemann G, Sterpone F, Hynes JT. Water Jump Reorientation: From Theoretical Prediction to Experimental Observation. *Accounts Chem Res* 2012, **45**(1)**:** 53-62.

7. Ni YC, Gruenbaum SM, Skinner JL. Slow hydrogen-bond switching dynamics at the water surface revealed by theoretical two-dimensional sum-frequency spectroscopy. *Proc Natl Acad Sci USA* 2013, **110**(6)**:** 1992-1998.

8. Ojha D, Kaliannan NK, Kuhne TD. Time-dependent vibrational sum-frequency generation spectroscopy of the air-water interface. *Commun Chem* 2019, **2**.

9. Inoue K, Nihonyanagi S, Singh PC, Yamaguchi S, Tahara T. 2D heterodyne-detected sum frequency generation study on the ultrafast vibrational dynamics of H_2O and HOD water at charged interfaces. *Journal of Chemical Physics* 2015, **142**(21).

10. Cyran JD, Backus EHG, Nagata Y, Bonn M. Structure from Dynamics: Vibrational Dynamics of Interfacial Water as a Probe of Aqueous Heterogeneity. *Journal of Physical Chemistry B* 2018, **122**(14)**:** 3667-3679.

11. Eigen M. Immeasurably Fast Reactions. *Nobel Lecture* 1967, **11:** 1963-1979.

12. Kirov MV. Atlas of optimal proton configurations of water clusters in the form of gas hydrate cavities. *J Struct Chem*+ 2002, **43**(5)**:** 790-797.

13. Yu Qi BMJ. Tracking Hydronium/Water Stretches in Magic $H_3O^+(H_2O)_{20}$ Clusters through High-level Quantum VSCF/VCI Calculations. *J Phys Chem A* 2020, **124**(6)**:** 1167-1175.

14. Fournier JA, Johnson CJ, Wolke CT, Weddle GH, Wolk AB, Johnson MA. Vibrational spectral signature of the proton defect in the three-dimensional $H^+\cdot(H_2O)_{21}$ cluster. *Science* 2014, **344**(6187)**:** 1009-1012.

15. Yang N, Duong CH, Kelleher PJ, McCoy AB, Johnson MA. Deconstructing Water's Diffuse OH Stretching Vibrational Spectrum With Cold Clusters. *Science* 2019, **364**(6437)**:** 275-278.

16. Yang N, Duong CH, Kelleher PJ, Johnson MA. Capturing Intrinsic Site-Dependent Spectral Signatures and Lifetimes of Isolated OH Oscillators in Extended Water Networks. *Nature Chem* 2019.

17. Yang N, Duong CH, Kelleher PJ, Johnson MA, McCoy AB. Isolation of Site-Specific Anharmonicities of Individual Water Molecules in the $I^-\cdot(H_2O)_2$ Complex Using Tag-Free, Isotopomer Selective IR-IR Double Resonance. *Chem Phys Lett* 2017, **690:** 159-171.

18. Wolke CT, Fournier JA, Miliordos E, Kathmann SM, Xantheas SS, Johnson MA. Isotopomer-Selective Spectra of a Single Intact H_2O Molecule in the $Cs^+(D_2O)_5H_2O$ Isotopologue: Going Beyond Pattern Recognition to Harvest the Structural Information Encoded in Vibrational Spectra. *J Chem Phys* 2016, **144**(7)**:** 074305.

19. Yang N, Duong CH, Kelleher PJ, Johnson MA. Unmasking Rare, Large-Amplitude Motions in D_2-Tagged $I^-\cdot(H_2O)_2$ Isotopomers with Two-Color, Infrared–Infrared Vibrational Predissociation Spectroscopy. *J Phys Chem Lett* 2018, **9**(13)**:** 3744-3750.

20. Yang N, Duong CH, Kelleher PJ, Johnson MA, McCoy AB. Isolation of site-specific anharmonicities of individual water molecules in the $I^-\cdot(H_2O)_2$ complex using tag-free, isotopomer selective IR-IR double resonance. *Chem Phys Lett* 2017, **690:** 159-171.

21. Yang N, Duong CH, Kelleher PJ, Johnson MA. Capturing intrinsic site-dependent spectral signatures and lifetimes of isolated OH oscillators in extended water networks. *Nat Chem* 2020, **12:** 159-164.

22. Boulon J, Braud I, Zamith S, Labastie P, L'Hermite JM. Experimental nanocalorimetry of protonated and deprotonated water clusters. *J Chem Phys* 2014, **140**(16).

23. Schmidt M, von Issendorff B. Gas-phase calorimetry of protonated water clusters. *Journal of Chemical Physics* 2012, **136**(16).

24. Dunbar RC. BIRD (blackbody infrared radiative dissociation): Evolution, principles, and applications. *Mass Spectrom Rev* 2004, **23**(2)**:** 127-158.

25. Niedner-Schatteburg G, Bondybey VE. FT-ICR studies of solvation effects in ionic water cluster reactions. *Chem Rev* 2000, **100**(11)**:** 4059-4086.

26. Calvo F, Douady J, Spiegelman F. Accurate evaporation rates of pure and doped water clusters in vacuum: A statistico-dynamical approach. *J Chem Phys* 2010, **132**(2).

27. Korchagina K, Simon A, Rapacioli M, Spiegelman F, L'Hermite JM, Braud I*, et al.* Theoretical Investigation of the Solid–Liquid Phase Transition in Protonated Water Clusters. *Phys Chem Chem Phys* 2017, **19**(40)**:** 27288-27298.

28. Stachl CN, Williams ER. Effects of Temperature on $Cs^+(H_2O)_{20}$ Clathrate Structure. *Journal of Physical Chemistry Letters* 2020, **11:** 6127-6132.

29. Magnera TF, David DE, Michl J. The 1st 28 Gas-Phase Proton Hydration Energies. *Chem Phys Lett* 1991, **182**(3-4)**:** 363-370.

30. Shi Z, Ford JV, Wei S, Castleman AW, Jr. Water clusters: contributions of binding energy and entropy to stability. *J Chem Phys* 1993, **99**(10)**:** 8009-8015.

31. Vazquez T, Taylor C, Evans-Nguyen T. Ion-Trap-Performance Enhancement Utilizing Pulsed Buffer-Gas Introduction. *Anal Chem* 2018, **90**(17)**:** 10600-10606.

32. Harrilal CP, DeBlase AF, Fischer JL, Lawler JT, McLuckey SA, Zwier TS. Infrared Population Transfer Spectroscopy of Cryo-Cooled Ions: Quantitative Tests of the Effects of Collisional Cooling on the Room Temperature Conformer Populations. *J Phys Chem A* 2018, **122**(8)**:** 2096-2107.

33. Rakshit A, Bandyopadhyay P, Heindel JP, Xantheas SS. Atlas of putative minima and low-lying energy networks of water clusters n = 3-25. *J Chem Phys* 2019, **151**(21)**:** 214307.

34. Kirov MV, Fanourgakis GS, Xantheas SS. Identifying the most stable networks in polyhedral water clusters. *Chemical Physics Letters* 2008, **461**(4-6)**:** 180-188.

35. March R.E. An introduction to quadrupole ion trap mass spectrometry. J Mass Spectrom , **32**(4), 351-369 (1997).

36. Xantheas S. S., Low-lying energy isomers and global minima of aqueous nanoclusters: Structures and spectroscopic features of the pentagonal dodecahedron $(H_2O)_{20}$ and $(H_3O)^+(H_2O)_{20}$. *Can. J. Chem. Eng.* **90**, 843-851 (2012).

37. Hodges M. P., Wales D. J., Global minima of protonated water clusters. *Chem. Phys. Lett.* **324**, 279-288 (2000).

38. Schütz M., Lindh R., Werner H. J., Integral-direct electron correlation methods. *Mol. Phys.* **96**, 719 (1999).

39. Azhary A. El, Rauhut G., Pulay P., Werner H. J., Analytical energy gradients for local second-order Møller-Plesset perturbation theory. *J. Chem. Phys.* **108**, 5185 (1998).

40. Werner H. J., Manby F. R., Knowles P. J., Fast linear scaling second-order Møller-Plesset perturbation theory (MP2) using local and density fitting approximations. *J. Chem. Phys.* **118**, 8149 (2003).

41. Polly R., Werner H. J., Manby F. R., Knowles Peter J., Fast Hartree-Fock theory using local density fitting approximations. *Mol. Phys.* **102**, 2311 (2004).

42. Møller C., Plesset M. S., Note on an approximation treatment for many-electron systems. *Phys. Rev.* **46**, 618– 622 (1934).

43. Eckert F., Pulay P., Werner H. J., *Ab initio* geometry optimization for large molecules. *J. Comp. Chem.* **18**, 1473 (1997).

44. Dunning T. H., Gaussian basis sets for use in correlated molecular calculations. I. The atoms boron through neon and hydrogen. *J. Chem. Phys.* **90**, 1007– 1023 (1989).

45. Kendall R. A., Dunning T. H., Harrison R. J., Electron affinities of the first-row atoms revisited. Systematic basis sets and wave functions. *J. Chem. Phys.* **96**, 6796– 6806 (1992).

46. Eichkorn K., Treutler O., Öhm H., Häser M., Ahlrichs R., Auxiliary basis sets to approximate Coulomb potentials. *Chem. Phys. Lett.* **240**, 283– 290 (1995).

47. Eichkorn K., Weigend F., Treutler O., Ahlrichs R., Auxiliary basis sets for main row atoms and transition metals and their use to approximate Coulomb potentials. *Theor. Chem. Acc.* **97**, 119–124 (1997).

48. Eichkorn K., Treutler O., Oehm H., Häser M., Ahlrichs R., Auxiliary basis sets to approximate Coulomb potentials. *Chem. Phys. Lett.* **240**, 283– 290 (1995).

49. Weigend F., Accurate Coulomb-fitting basis sets for H to Rn. *Phys. Chem. Chem. Phys.* **8**, 1057–1065 (2006).

50. Hrenar T., Rauhut G., Werner H. J., Impact of local and density fitting approximations on harmonic vibrational frequencies. *J. Phys. Chem. A* **110**, 2060 (2006).

51. Werner H. J., Knowles P. J., Knizia G., Manby F. Schutz R., M., Molpro: a general-purpose quantum chemistry program package. WIREs Comput. *Mol. Sci*. **2**, 242– 253. (2012).

52. Werner H. J., Knowles P. J., Knizia G., Manby F. R., Schütz M., Celani P., Györffy W., Kats D., Korona T., Lindh R., MOLPRO, version 2019.1, a package of ab initio programs. (2019).

53. Lagutchenkov A., Fanourgakis G. S., Xantheas S. S., *J. Chem. Phys.* **122**, 194310 (2005).

54. Schlegel, Verh. Kais. Leopold.-Carolin V. . *Dtsch. Akad. Naturforsch* **44**, 343 (1883).

55. Babin, V., Leforestier, C. & Paesani, F. Development of a "First Principles" Water Potential with Flexible Monomers: Dimer Potential Energy Surface, VRT Spectrum, and Second Virial Coefficient. *Journal of Chemical Theory and Computation* **9**, 5395-5403 (2013).

56. Wales, D. OPTIM: A program for optimizing geometries and calculating reaction pathways, http://www-wales.ch.cam.ac.uk/OPTIM/.

57. Fanourgakis, G. S. & Xantheas, S. S. The flexible, polarizable, Thole-type interaction potential for water (TTM2-F) revisited. *J. Phys. Chem. A* **110**, 4100-4106 (2006).